Combined MR, fluorescence and histology imaging strategy in a human breast tumor xenograft model

Lu Jiang[a], Tiffany R. Greenwood[a], Erika R. Amstalden van Hove[b], Kamila Chughtai[b], Venu Raman[a,c], Paul T. Winnard Jr[a], Ron M. A. Heeren[b], Dmitri Artemov[a,c] and Kristine Glunde[a,c]*

Applications of molecular imaging in cancer and other diseases frequently require the combination of *in vivo* imaging modalities, such as MR and optical imaging, with *ex vivo* optical, fluorescence, histology and immunohistochemical imaging to investigate and relate molecular and biological processes to imaging parameters within the same region of interest. We have developed a multimodal image reconstruction and fusion framework that accurately combines *in vivo* MRI and MRSI, *ex vivo* brightfield and fluorescence microscopic imaging and *ex vivo* histology imaging. *Ex vivo* brightfield microscopic imaging was used as an intermediate modality to facilitate the ultimate link between *ex vivo* histology and *in vivo* MRI/MRSI. Tissue sectioning necessary for optical and histology imaging required the generation of a three-dimensional reconstruction module for two-dimensional *ex vivo* optical and histology imaging data. We developed an external fiducial marker-based three-dimensional reconstruction method, which was able to fuse optical brightfield and fluorescence with histology imaging data. The registration of the three-dimensional tumor shape was pursued to combine *in vivo* MRI/MRSI and *ex vivo* optical brightfield and fluorescence imaging data. This registration strategy was applied to *in vivo* MRI/MRSI, *ex vivo* optical brightfield/fluorescence and histology imaging datasets obtained from human breast tumor models. Three-dimensional human breast tumor datasets were successfully reconstructed and fused with this platform.

Keywords: molecular imaging; cancer; multimodal; MRI; MRSI; fluorescence; histology; fiducial marker

INTRODUCTION

The investigation of complex diseases, such as cancer, often requires the combined use of different *in vivo* imaging modalities, such as MRI, MRSI and optical imaging applications, with *ex vivo* histologic analyses obtained with optical microscopy. In most studies, a combined molecular–functional–anatomic imaging approach provides the maximum benefit, but requires a combination of multiple imaging modalities, as each modality has strengths and weaknesses (1,2).

MRI is useful for the noninvasive measurement of the three-dimensional (3D) anatomic structure of an organ or tissue of interest when performing the characterization of regional pathology (3). With the use of gadolinium-containing contrast agents of different sizes, such as clinically approved gadopentetate dimeglumine (Magnevist) or preclinically used albumin gadolinium diethylenetriamine pentaacetic acid (4), contrast-enhanced MRI can be performed to assess vascular volume, the permeability of blood vessels and contrast agent transport across the extracellular matrix (5) noninvasively in three dimensions. Such MRI techniques provide a wealth of functional information, but are limited by their relatively low sensitivity of detection and low spatial resolution compared with *ex vivo* techniques. In addition, molecular targeted MRI contrast agents for receptor imaging are often quite large, with a diameter between 30 and 200 nm, which can limit the delivery of these contrast agents to the tumor tissue (6). MRSI is able to noninvasively detect the 3D spatial distribution of endogenous metabolites *in vivo*; however, its low sensitivity results in low spatial resolution (7). Recent advances have expanded MRI/MRSI towards the characterization of functional tumor parameters, such as intra- and extracellular pH, as well as tissue levels of glucose, choline and lipid, and markers of energy metabolism, such as adenosine triphosphate

and phosphocreatine (7–11). However, in studies that are geared towards the elucidation of molecular pathways, it is often necessary to obtain additional information from complementary imaging modalities, which are often performed *ex vivo*.

Ex vivo optical imaging, including fluorescence and bioluminescence imaging, plays a crucial role in modeling different human diseases because of its high specificity, sensitivity and spatial resolution. Optical imaging can be used to image transcription factors, such as hypoxia-inducible factor 1 (12), receptors such as HER-2 or $\alpha_v\beta_3$ (13–15), different activated oncogenes, such as p53 and myc (16), and activated enzymes with activatable probes for cathepsin D, cathepsin B and matrix metalloproteinase 2 (17–19), as well as the tracking of cells that express fluorescent proteins or luciferases in cancer invasion and metastasis (20). The majority of optical imaging systems to date generate only two-dimensional (2D) images of the integrated light distribution emitted from the surface of the 3D tissue, which severely compromises the ability to quantify and accurately localize these optical signals because of their strong dependence on optical tissue properties and depth (1). There is great interest in developing fluorescence and bioluminescence imaging applications that generate volumetric images, such as diffuse optical tomography and fluorescence laminar optical tomography, which accurately localize signals and enable quantitative studies of fluorescent contrast agents and proteins (21–23). Such developments in optical imaging instrumentation/applications will potentially result in higher temporal and spatial resolution (1). However, many research applications to date use optical imaging of 2D tissue sections instead of technically challenging 3D optical imaging (22), which necessitates 3D reconstruction.

Immunohistochemical (IHC) staining analyses, such as the staining of HER-2/neu, estrogen receptor and progesterone receptor, and histologic staining of nuclei with hematoxylin and matrix with eosin, are usually performed on 5–10-μm-thick tissue cryosections or formaldehyde/formalin-fixed paraffin-embedded sections to visualize receptor expression, and nuclear and tissue morphology (24). Histology and IHC imaging provide high sensitivity and high spatial resolution of detection in cancer diagnosis and treatment. However, like most other optical imaging modalities, histology and IHC imaging can only generate 2D images of stained thin tissue sections. As a result, samples typically need to be cryosectioned all the way through the tissue of interest, and multiple 2D images need to be examined to draw conclusions. Reconstruction in three dimensions of such histology and IHC images would aid in the visualization of the spatial distribution of the stained molecular features in three dimensions, thereby avoiding the restriction of investigating only one 2D section at a time.

A recent study has reported a Teflon fiducial template which allows the insertion of small hollow Teflon rods of ~0.71 mm in diameter into the tumor (25,26). Using this approach, image registration was performed for MRI and digitized microscopy images of tissue histology based on the rigid Teflon rods. More recently, two iridescent acrylic paints, 'bronze' and 'stainless steel', have been evaluated to fuse 3D MRI and histology images, and a straight-line paint-track fiducial method has been developed to assist in registration and 3D histopathology reconstruction (27). These two methods propose different solutions towards the fusion of MRI and histology datasets, without providing the option of adding other optical imaging datasets of the same tumor, e.g. as an intermediate imaging modality. Breen *et al*. (28) have developed a 3D registration method of MRI data for histologic sections of rabbit thigh using macroscopic tissue as the reference. Fiducial markers embedded in surrounding tissue were employed in their method. However, breast tumor xenografts grown in the mammary fat pad of mice, similar to many other preclinical tumor models and certain clinical tumors, do not contain large amounts of surrounding tissue, and therefore it would not be feasible to place fiducial markers in close proximity to the tumor *in vivo* without contaminating and injuring the tumor tissue. Injuring tissue close to a tumor can also have undesirable effects on tumor vascularization. The size of the surface coil, which is typically used for imaging mouse breast tumor in preclinical MRI scanners, also limits the space for placing fiducial markers *in vivo*.

Other studies (29–33) on the registration of histologic slices and *in vivo* MRI for primate brain, which, unlike tumor xenograft tissue, provides ample anatomical features for co-registration, have also been performed. The individual 2D deformation for each slice as a result of cutting and shrinkage was corrected by introducing an intermediate modality, which is obtained through blockface photographs. This series of blockface photographs consists of photographs of the brain surface taken at different steps during the sectioning process. Both global affine transform and nonlinear transformation were performed on the alignment of this series of 2D slices (34,35). Compared with primate brain tissue with skull, less rigid transformation occurs in mouse breast tissue during sectioning. As a result, external fiducial markers are more feasible to provide accurate 3D reconstruction and registration of histology in breast tumors, which are tissues that do not contain distinct landmark structures.

To address these 3D reconstruction and registration needs, we developed an external fiducial marker strategy that does not interfere with the tumor tissue, and an image reconstruction and fusion framework for multimodal MRI/MRSI, brightfield/fluorescence imaging and histology imaging.

MATERIALS AND METHODS

To illustrate the workflow and buildup of our novel platform, we performed *in vivo* MRI/MRSI, *ex vivo* optical brightfield and fluorescence imaging, and histology imaging of an orthotopic breast tumor xenograft model, which is derived from cells that express tdTomato fluorescent protein in hypoxic regions of the tumor, as shown in Fig. 1.

Breast tumor model

The MDA-MB-231 breast cancer cell line purchased from the American Type Culture Collection (ATCC, Manassas, VA, USA) was used in this study. Cell culture of this cell line was performed as described previously (36). MDA-MB-231 breast cancer cells were genetically modified to express tdTomato red fluorescent protein under the control of a promoter containing a tandem repeat of five hypoxia-response elements (HREs) (MDA-MB-231-HRE-tdTomato) (37–39). MDA-MB-231-HRE-tdTomato breast tumor xenografts were obtained by inoculating 2×10^6 MDA-MB-231-HRE-tdTomato breast cancer cells in 0.05 mL Hank's balanced salt solution (Sigma, St. Louis, MO, USA) into the upper left thoracic mammary fat pad of female athymic Nu/Nu nude mice (NCI-Frederick, Cat. 01B74, Frederick, MD). Mice weighed between 24 and 28 g and tumor sizes were $(8.0 \pm 0.4\,\text{mm}) \times (8.0 \pm 0.4\,\text{mm}) \times (8.0 \pm 0.4\,\text{mm})$ when experiments were performed. All experimental animal protocols were approved by the Institutional Animal Care and Use Committee of the Johns Hopkins University School of Medicine.

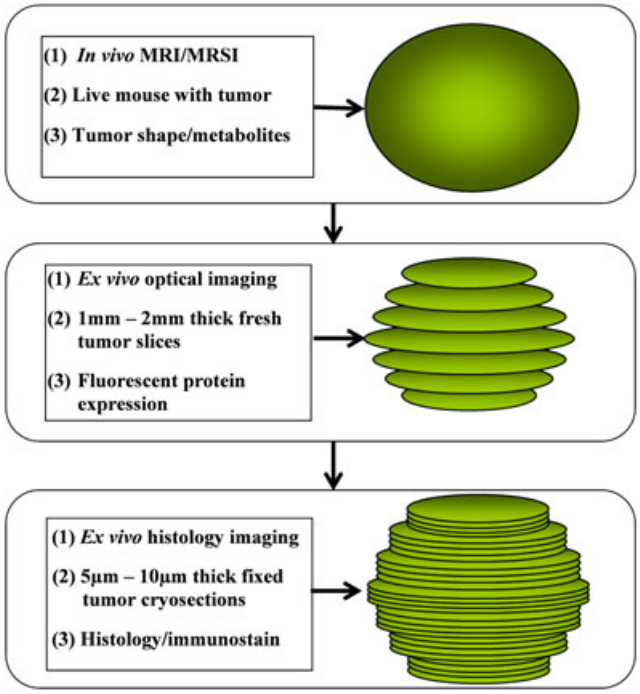

Figure 1. Schematic overview of the presented multimodal imaging approach using *in vivo* MRI/MRSI, *ex vivo* optical brightfield/fluorescence imaging and histology imaging.

3D *in vivo* T_1-weighted MRI and MRSI

All mice were scanned *in vivo* on a 9.4-T Bruker Avance Small Animal MR Scanner (Bruker, Billerica, MA, USA) in the Broadway Research Building Molecular Imaging Center at the Johns Hopkins University School of Medicine. 3D MRSI images were obtained, together with the corresponding high-resolution 3D T_1-weighted MRI data, which served as high-resolution anatomic reference image datasets for the 3D MRSI data.

Tumor-bearing mice were anesthetized by intraperitoneal injection of ketamine (25 mg/kg; Phoenix Scientific, Inc., Encinitas, CA) and acepromazine (2.5 mg/kg; Aveco, Phoenix Scientific Inc., Encinitas, CA) diluted in saline. The tumors of anesthetized mice were placed inside a home-built ^{1}H cylinder surface coil of about 13 mm in diameter, and this set-up was mounted on a heated cradle to keep the animal warm. We used a 3D rapid acquisition with relaxation enhancement (RARE) spin echo fast imaging sequence to acquire 3D T_1-weighted images. RARE acquires multiple spin echoes using the Carr–Purcell–Meiboom–Gill sequence (40,41) with slice-selective radiofrequency pulses. 3D RARE was performed with the following parameters: TE = 7.2 ms; TR = 500 ms; RARE factor, 4; flip angle, 90°; field of view (FOV), 1.0 cm × 1.0 cm × 1.0 cm; 64 phase encode steps (64 × 64 × 64 voxels); number of averages, 4. The total acquisition time was 13 min. The reconstruction of MRI reference images was performed using ParaVision 5.0 software (Bruker Co., Billerica, MA), and magnitude 3D MRI reference images were imported into our novel multimodal molecular imaging reconstruction and fusion platform to generate a series of 2D images.

MRSI was achieved using a 3D spin echo chemical shift imaging sequence (42). Water-suppressed MRSI was performed using VAPOR (43) with the same geometry as used for the corresponding 3D RARE acquisition, with the following parameters: Gaussian excitation pulse length, 0.25 ms; flip angle, 90°; TE = 82 ms; TR = 1000 ms; spectral resolution, 3.9 Hz/point; sweep width, 4000 Hz; FOV, 1.0 cm × 1.0 cm × 1.0 cm. The diameter of our cylinder surface coil is 13 mm, which is slightly larger than the size of the mouse breast tumor xenograft. Most of the tumor was placed inside of the coil, which makes the B_1 pulse profile of the Gaussian excitation pulse sufficiently strong to reach a 90° flip angle. Rectangular *k*-space sampling was used with a matrix size of 8 × 8 × 8 (zero filled to 64 × 64 × 64), and number of averages of four, resulting in a total measurement time of 33 min. An in-house IDL program was developed to reconstruct water-suppressed MRS images. This software performed Fourier transformations over both the spatial axis and spectral axis of MRSI raw data, and automatically detected all metabolite peaks by applying a sliding window across the whole spectral range with a window width of 0.3 ppm and a step size of 0.3 ppm. A signal-to-noise ratio threshold was applied to the water-suppressed MRSI data to detect metabolite peaks. The signal-to-noise ratio threshold was set to three in this study. Following these MRI/MRSI studies, mice were sacrificed, and each tumor was fiducially marked and sectioned as described below.

Fiducial marker application

Prior to starting the tumor preparation, 4 g of gelatin Type A from porcine skin (Sigma, Cat. G-2500, St. Louis, MO) was dissolved in 40 mL of distilled water warmed to 37 °C to create a 10% gelatin solution. Five micrograms of Ponceau S Practical Grade (Sigma, Cat. P3504-10 G, St. Louis, MO) was dissolved in 1 mL of 10% gelatin solution to create the fiducial marker solution. Both solutions are liquid at 37 °C and solidify to form a gel at room temperature.

Following *in vivo* MRI/MRSI, each mouse was sacrificed by the cervical dislocation method, and the tumor was immediately removed and placed in a Disposable Vinyl Specimen Cryomold (Fisher Scientific, Pittsburg, PA Cat. 4566) containing sufficient liquid gelatin to immerse the tumor. The original tumor orientation was preserved as indicated in Fig. 2A. The top portion is defined as the upper region of the tumor located furthest away from the rib cage, the center region is defined as the middle region, and the body wall is the region located just adjacent to the rib cage. Three to four 25-mm pieces of 1.57-mm-thick Intramedic Non-Radiopaque Non-Toxic Polyethylene Tubing (Clay Adams, Becton Dickinson, Franklin Lakes, NJ Cat. 7431) were immediately placed in either a diagonal or vertical arrangement in the space surrounding the gelatin-immersed tumor (see Fig. 2C). This step is essential for the creation of holes in which the fiducial markers will later be inserted. The cryomold containing the 10%-gelatin-embedded tumor and tubing was placed on a 20-mL weigh boat (VWR International, Radnor, PA Cat. 12577–005) over a bath of liquid nitrogen to solidify the gelatin whilst keeping the tubing in place. The embedded tissue was removed from cooling over liquid nitrogen just prior to the gelatin turning white. The tubing was then removed from the cryomold. A 1-mL latex-free syringe (Becton Dickinson, Franklin Lakes, NJ, Cat. 309625) with a 20 G × 1½ precision guide needle (Becton Dickinson, Franklin Lakes, NJ, Cat. 305176) filled with the fiducial marker was warmed to 37 °C and fiducial markers were injected into the holes left by the tubing (see Fig. 2D), and re-cooled over liquid nitrogen to solidify the fiducial markers. The gelatin-embedded tumor with fiducial markers was then extracted from the cryomold (see Fig. 2E) and placed in the tissue slicer. Two-mm-thick slices were cut and placed on ice-cold glass slides (Fisherbrand catalog number 12-550-34; Fisher Scientific, Pittsburg, PA, USA) over ice in an arrangement that preserved the orientation.

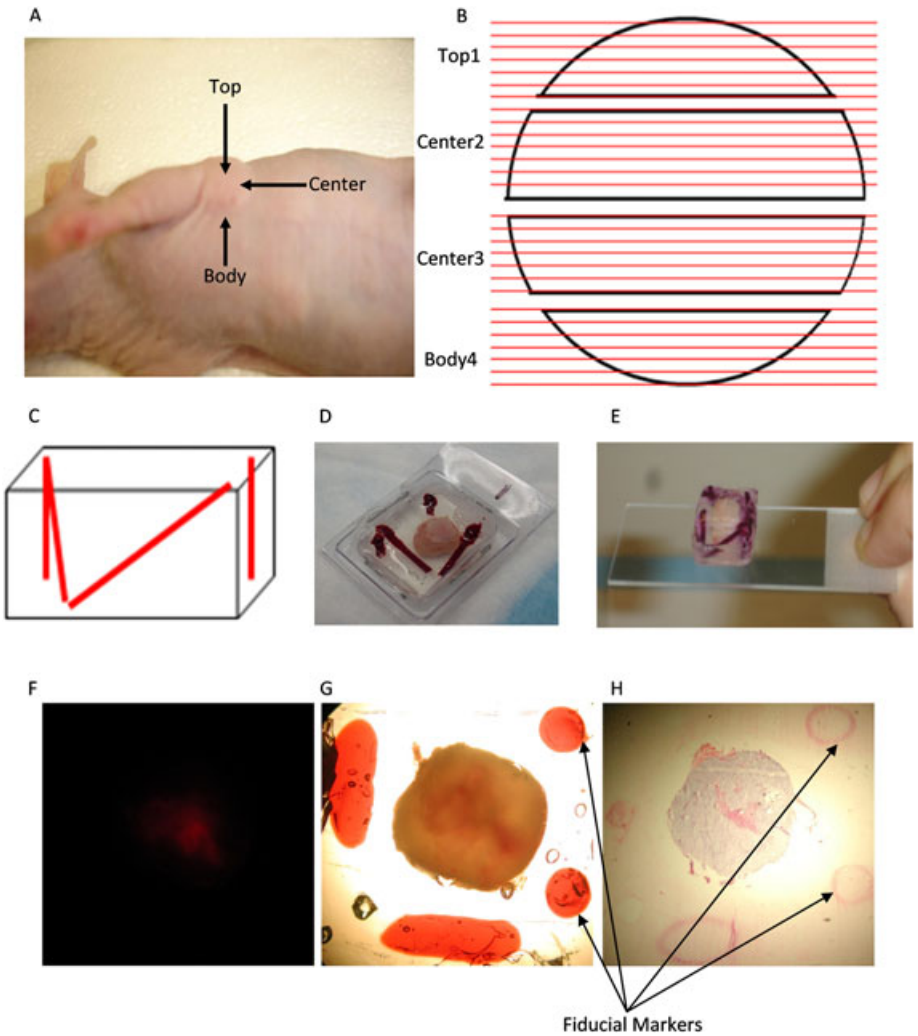

Figure 2. (A) Definition of the top, center and body portions of a mouse breast tumor xenograft. (B) Diagram describing the sectioning of the tumor from top to body. Black outlines: top first slice, center second slice, center third slice and body fourth slice. Red lines: each 2-mm slice was sectioned into 5–10-μm cryosections and stained with hematoxylin and eosin (H&E). (C) Diagram depicting two diagonal markers and two straight markers. (D) Extracted tumor embedded in gelatin with two diagonal markers and two straight markers in the cryomold. (E) Extracted tumor embedded in gelatin with markers after taking away the cryomold placed on the microscope slide. (F) Fluorescence microscopic image (1× objective) from a 2-mm-thick tissue slice of a MDA-MB-231-HRE-tdTomato breast tumor. (G) Brightfield microscopic images (1× magnification) of the same field of view from a 2-mm-thick tissue slice of a MDA-MB-231-HRE-tdTomato breast tumor with two straight circular shape and two diagonal elliptic shape fiducial markers. (H) Corresponding microscopic H&E histology image (1× objective) from a 10-μm-thick tissue section of a MDA-MB-231-HRE-tdTomato breast tumor with two straight circular shape and one diagonal elliptic shape fiducial markers.

These fresh tissue slices matched the 3D MRI/MRSI image datasets in terms of geometry. This procedure from the time of tumor extraction to the time of microscopic imaging took no longer than 20 min, and tissue was kept on ice to avoid tissue degradation.

Ex vivo brightfield and fluorescence microscopy imaging

For microscopic measurements, a given slide holding an embedded, fiducially marked fresh tumor slice was taken out of the icebox and placed under the microscope for imaging. Each slice was carefully positioned so that the entire tumor and all of the adjacent fiducial markers were included in the image. In between microscopic measurements, the fresh tumor slices were returned to the icebox to keep the tissue at 4 °C, and they were periodically moistened with saline to avoid dehydration of the tissue. Fluorescence microscopy images were obtained using a 1× objective attached to a Nikon microscope, equipped with a filter set for 528–553-nm excitation and 600–660-nm emission and a Nikon Coolpix digital camera (Nikon Instruments, Inc., Melville, NY). Brightfield images of the same FOV were acquired by the same microscope to obtain the tumor slice shape and fiducial markers. The fiducial markers were clearly visible in the brightfield images, which were inherently registered with the corresponding fluorescence images (Fig. 2F, G). Following microscopy, the embedded samples where cooled over liquid nitrogen until the gelatin turned white. Samples were stored in a −80 °C freezer until cryosectioning was performed.

Histology imaging

The frozen gelatin-embedded tumor slices were cryosectioned on a Microm HM550 cryostat microtome (Microm International

GmbH, Walldorf, Germany). Sets of contiguous 10-μm-thick cryosections were cut across the tumor from the top to the body wall throughout all 2-mm-thick gelatin-embedded slices (see Fig. 2B) with a distance of 500 μm in between, and the first and last 100-μm-thick cryosections were discarded. Sections were attached to Superfrost Slides (VWR International, Radnor, PA, Cat. 48311–600), washed with 1 × phosphate-buffered saline and fixed immediately in 3% paraformaldehyde for 30 min. Fixed tissue sections were placed in a glass Coplin jar containing 40 mL of distilled water and then in a separate Coplin jar of Mayer's hematoxylin (Sigma, St. Louis, MO Cat. 51275) for 30 min. Sections were gently washed in distilled water five times. To avoid drying, sections were immediately immersed in a jar containing 40 mL eosin Y, aqueous, 1% PDC (EMD Chemicals Inc., Billerica, MA, Cat. 592–75) for 30 min, followed by five washes with distilled water. Fixed and stained tissue sections were dehydrated by submersion in 200-proof ethyl alcohol (The Warner-Graham Company, Cockeysville, MD, Cat. 64-17-5) twice for 3 min each. Sections were immersed in a jar containing 40 mL of Histo-Clear II (National Diagnostics, Atlanta, GA, Cat. HS 202) twice for 2 min each, followed by mounting with Richard–Allen Cytoseal 60 Mounting Medium (Thermo Scientific, Waltham, MA, Cat. 8310–4). A coverslip was immediately applied and sections were dried at room temperature for 24 h prior to imaging. Brightfield images were obtained using a 1× objective attached to a Nikon microscope, equipped with a Nikon Coolpix digital camera (Nikon Instruments, Inc. Melville, NY). The fiducial markers were clearly visible in the hematoxylin and eosin (H&E)-stained sections, as shown in Fig. 2H. Based on the H&E staining, dark purple tumor regions with intact nuclei were identified as viable tumor regions, and pink areas without nuclei were identified as necrotic tumor regions.

Platform of combined MRI/MRSI and multiparametric optical imaging

The workflow of our software platform, which combines MRI/MRSI and optical imaging (brightfield, fluorescence and histology imaging), is illustrated in Fig. 3. This software workflow was developed in Matlab 2009a (Natick, MA, USA). It has two modules of 3D reconstruction, including optical imaging reconstruction (Fig. 3A) and histology imaging reconstruction (Fig. 3B), and two modules of 3D hierarchical registration, including registration of MRI/MRSI with optical brightfield and fluorescence imaging (Fig. 3C), and registration of optical brightfield and fluorescence imaging with histology imaging (Fig. 3D). In the 3D reconstruction module, a fiducial marker-based 3D reconstruction method was utilized. The 3D hierarchical registration module included two steps. First, a fiducial marker-based rigid registration strategy was performed to fuse *ex vivo* optical brightfield and fluorescence images with *ex vivo* histology images. Second, a combined 3D tumor shape-based rigid and nonrigid registration strategy, considering both global translations and scaling as well as local deformations of tumor sections, was developed to combine *in vivo* MRI/MRSI images with *ex vivo* optical brightfield and fluorescence images and histology images.

Fiducial marker-based 3D reconstruction of optical images

The straight markers were used to align the microscopic images, and the diagonal markers were applied to check the order of the slices from the top portion to the body wall. Figure 4 illustrates the procedure of this fiducial marker-based 3D reconstruction of optical images. It was performed as follows. First, a rigid affine transformation derived from the centroid of each straight fiducial marker was applied to align the top, center and body sections (Fig. 4A). An affine transformation is composed of linear transformations (rotation and scaling) and a translation (or 'shift'). The top slice was used as a reference map, and the affine transformation was generated by measuring the centroid coordinates of the corresponding straight fiducial markers on both top and center slices. An aligned center section relative to the top slice was generated by applying this affine transformation to the original center section. The same method was utilized for additional center sections and the body section. The centroid

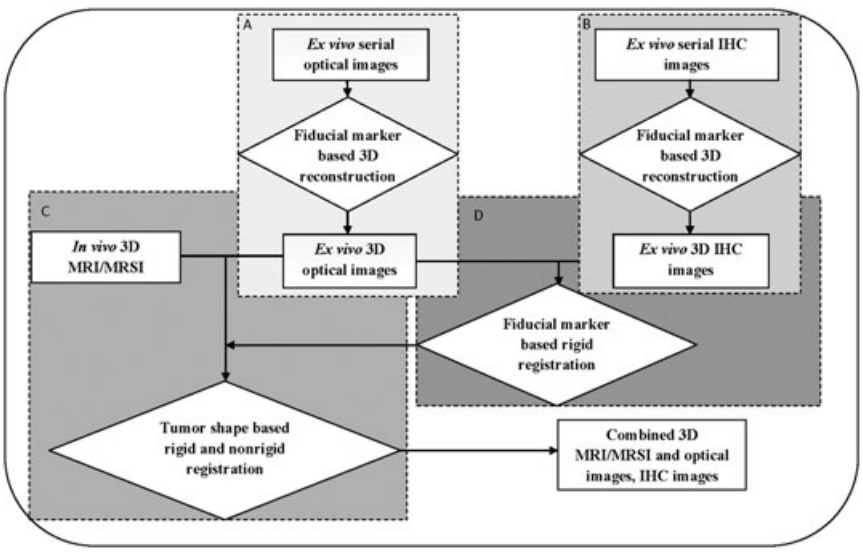

Figure 3. Workflow of combined three-dimensional (3D) *in vivo* MRI/MRSI and *ex vivo* optical and histology imaging, which consists of several modules: (A) optical imaging reconstruction; (B) histology imaging reconstruction; (C) 3D hierarchical registration of MRI/MRSI with optical brightfield and fluorescence imaging; (D) 3D hierarchical registration of optical brightfield and fluorescence imaging with histology imaging. All modules (A)–(D) are labeled in color from light gray to dark gray in order. Rectangular boxes represent different imaging modality data; diamond-shaped boxes represent different image processing steps. IHC, immunohistochemistry.

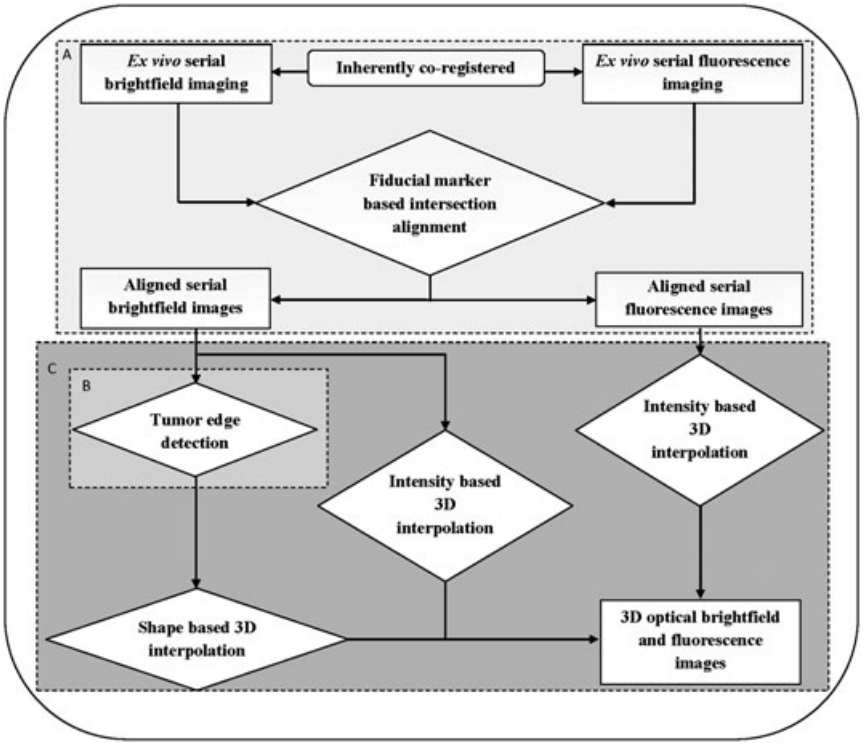

Figure 4. Workflow diagram of fiducial marker-based three-dimensional (3D) reconstruction of *ex vivo* optical brightfield and fluorescence imaging, which consists of several modules: (A) alignment of tumor sections; (B) tumor edge detection; (C) 3D combined shape and intensity-based interpolation. All modules (A)–(C) are labeled in color from light gray to dark gray in order. Rectangular boxes represent different imaging modality data; diamond-shaped boxes represent different image processing steps.

of each straight fiducial marker was picked manually in this software platform.

Second, an active shape model ('snake' or ASM) was utilized to detect the tumor edge in the aligned sections (44–46) (Fig. 4B). ASM is a statistical model of the shape of objects that iteratively deform to fit to the shape of the object in a new image. The shape of the tumor is represented by a set of points controlled by the shape model. The snake model in the Gradient Vector Flow Active Contour Toolbox (47) written in Matlab was used in this step. The parameter settings of our snake model were as follows: elasticity, 0.05; rigidity, 0; viscosity, 2.5; external force weight, 1.5; pressure force weight, 0.1; maximum number of iterations, 50. The initial tumor boundary points were manually selected for the ASM calculation.

Finally, a 3D combined shape and intensity-based interpolation was performed to render the 3D data of the tumor slices (48,49) (Fig. 4C). A tessellation-based 3D linear interpolation method was used for the shape-based interpolation. This method performs Delaunay 3D tessellation (50,51) to find values between neighboring points to be used for interpolation, which can help to speed up the search for neighboring points. 3D linear interpolation was also applied to the image intensity, and the shape interpolation was used as a mask for the intensity interpolation to generate the 3D volume of the tumor in brightfield images and the 3D spatial fluorescence intensity distribution in fluorescence images.

Co-registration procedure for MRI/MRSI, optical and histologic data

Histologic image sections were registered to the optical microscopic image sections by aligning the fiducial markers that were visible in both types of image, and rendered to give 3D registered histology images. The centroid of each fiducial marker in each corresponding histology and optical image section was manually selected in this platform. Figure 5 illustrates our workflow of fusing these three different imaging datasets – MRI/MRSI images, optical brightfield and fluorescence images, and histologic images of the breast tumor sections. The corresponding tumor boundary points were manually selected in the detected MRI tumor edge, excluding skin, which were detected by the ASM with the following parameters: elasticity, 0.02; rigidity, 0.01; viscosity, 2; external force weight, 1.8; pressure force weight, 0.1; maximum number of iterations, 50. The corresponding microscopic tumor edge images were both detected by the ASM (44–46). An affine transform was applied based on the boundary points to obtain rigid registered 3D microscopic brightfield images and MR images. As outlined in Fig. 5, *b*-spline-based warping (52–54) was performed between rigid registered 3D microscopic brightfield images and 3D MRI images to obtain warped 3D microscopic brightfield images. It is necessary to warp the rigid registered microscopic images because tissue may experience shear force and local deformation during sectioning. As the brightfield and fluorescence images were inherently co-registered, and were co-registered with histology images by our fiducial marker scheme, the same spatial affine transformations and the same *b*-spline-based nonrigid transformations as for the 3D microscopic brightfield images were applied to these 3D microscopic fluorescence and histology images. As the position of the mouse was kept the same during MRI/MRSI acquisition, and the geometry parameters of MRI RARE images and MRSI images were the same, the MRSI and MRI RARE images were co-registered. By comparing the relatively low spatial

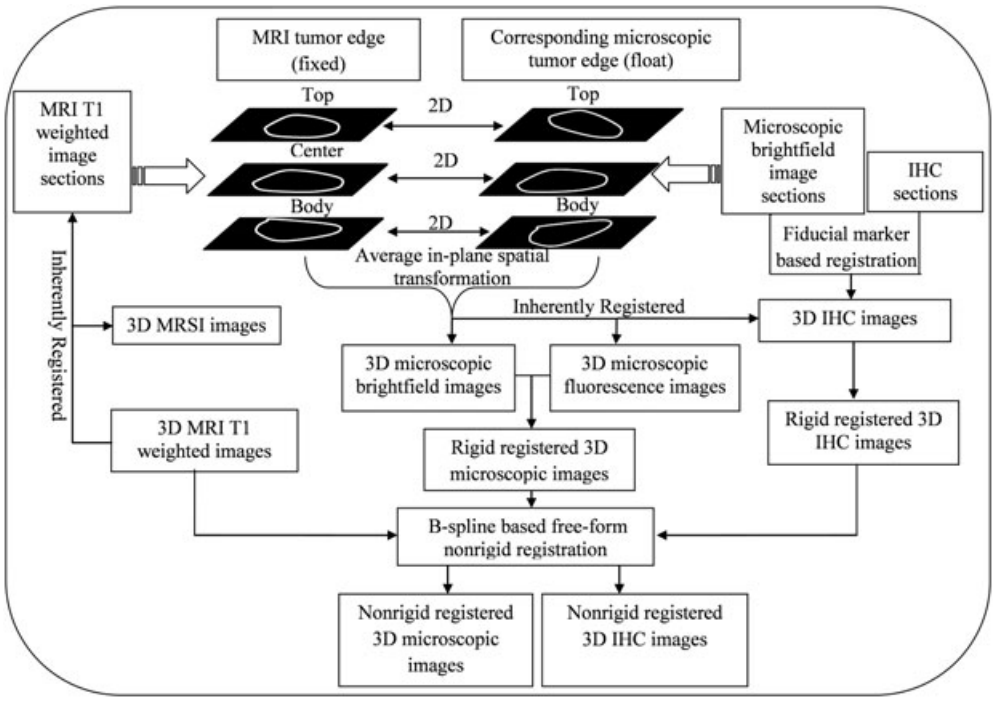

Figure 5. Schematic map of three-dimensional (3D) co-registration of optical fresh tissue brightfield/fluorescence imaging and histology with MRI/MRSI imaging data. IHC, immunohistochemistry.

resolution of MRSI ($8 \times 8 \times 8$) with the high spatial resolution of MRI ($64 \times 64 \times 64$), 8 voxels $\times$ 8 voxels $\times$ 8 voxels shifting was observed in a phantom with unique geometry as a result of asymmetric sampling in *k* space, and this shift was corrected in the MRSI images. The registered optical brightfield, fluorescence and histology images were co-registered with MRSI automatically after the fusion of MRI, optical imaging and histology was completed. The software Amira 5.2.1 (Mercury Computer Systems, Chelmsford, MA, USA) was used for 3D image display in this study.

Normalized mutual information (55) was used as a metric to measure the image difference in this study. The measurement of normalized mutual information, originating from information theory, is a measure of the statistical dependence between two datasets, which is particularly suitable for the registration of images from different modalities. The image difference error between the MRI image *M* and the optical image *O* used in this measurement was defined as follows:

$$\mathrm{Im}_{\mathrm{diff}_{error}} = 2 - \frac{H(M) + H(O)}{H(M,O)} \qquad [1]$$

where $H(.) = -\sum(p(.) \bullet \log p(.))$, $H(M)$ and $H(O)$ are the entropies of the MRI images *M* and the optical images *O*, and $H(M,O)$ is the joint entropy between these two image types. $p(.)$ is the normalized histogram of the MRI images *M*, optical images *O* or the normalized joint histogram of the MRI images *M* and optical images *O*. As the joint entropy decreases, the distance error will be minimized. The common measurement unit of entropy in information theory is the 'bit'. However, the normalized mutual information-based image distance error has no unit because of the cancelation of this unit in the denominator and numerator in the equation.

RESULTS

The application of our multimodal image reconstruction, registration and fusion platform worked well for 2-mm-thick fresh tumor slices that were imaged with brightfield and fluorescence microscopy, as shown in Fig. 6. The original brightfield images with fiducial markers are shown in Fig. 6A from the top of the tumor to the body wall. Each slice was 2 mm thick. Figure 6B demonstrates that the three serial slices from the top of the tumor to the body wall were aligned well by the fiducial markers. In Fig. 6C, tumor edge detection was successfully performed using the ASM as described in the Materials and methods section. The 3D tumor shape was interpolated to fill in values in between the 2-mm-thick slices, and the fluorescence intensity indicating hypoxic regions was interpolated accordingly using intensity interpolation (Fig. 6D). The serial slices with both tumor boundary and fluorescence intensity information were rendered after performing the combined 3D shape and intensity interpolation. Figure 6E shows the final 3D reconstructed tumor boundary as a yellow grid, with the hypoxic volume obtained from the red fluorescence signal shown in red.

The 3D reconstruction of H&E-stained histology images, including the corresponding intermediate results, is displayed in Fig. 7. The 3D reconstruction of histology images was performed analogous to that of the brightfield and fluorescence images shown in Fig. 6. Figure 7A presents the aligned fiducial markers and the corresponding 10-μm-thick tissue cryosections of H&E staining. Figure 7B shows the boundary of necrotic regions detected by ASM. Figure 7C demonstrates the rendered volume of necrotic tumor regions. Figure 7D shows the final 3D display of the reconstructed tumor shape (yellow grids) and necrotic regions (bright yellow color).

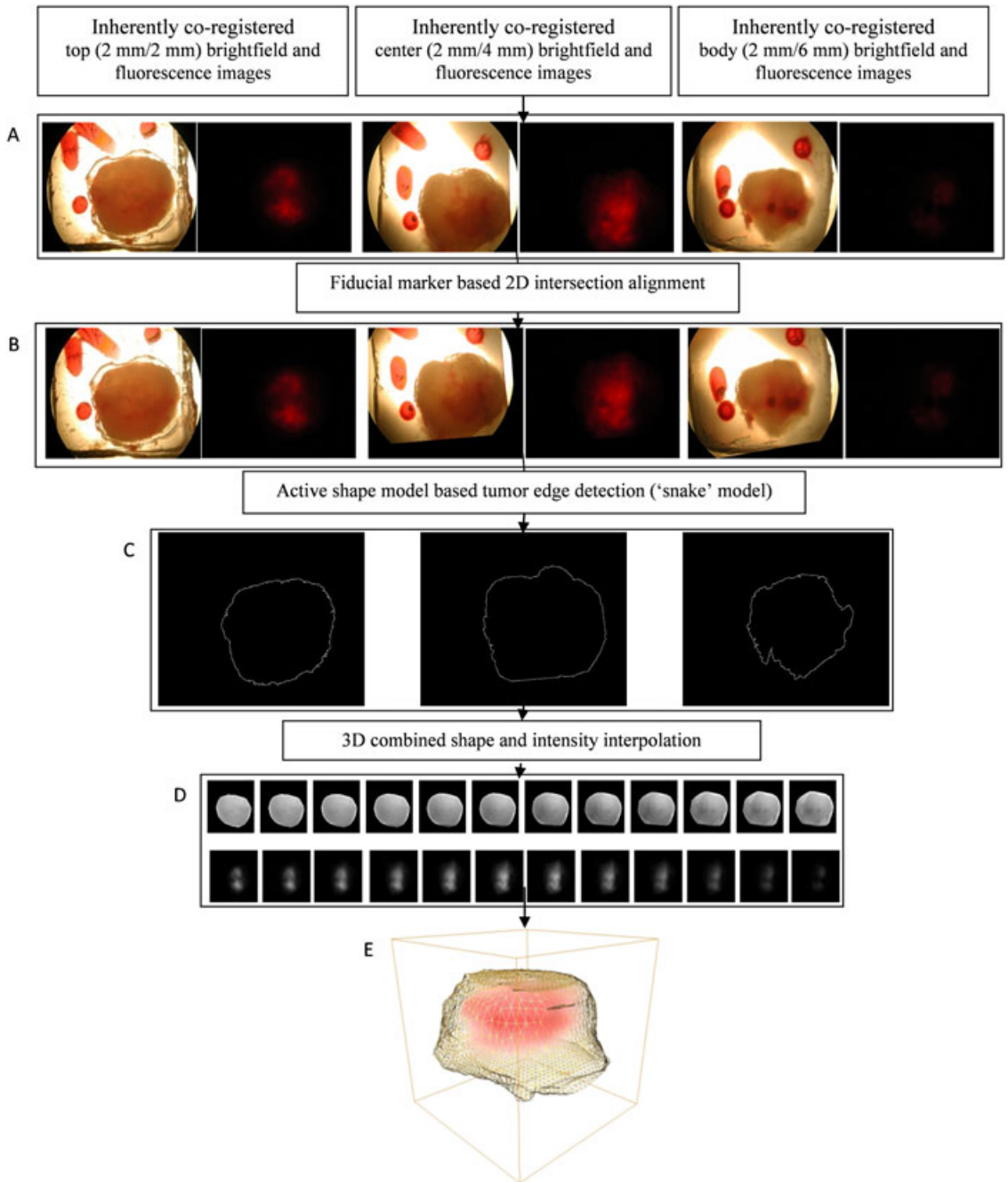

Figure 6. Results of three-dimensional (3D) reconstruction of optical brightfield and fluorescence images of 2-mm-thick tumor slices. (A) Original brightfield and fluorescence serial sections. (B) Brightfield and fluorescence serial sections after fiducial marker-based intersectional alignment. (C) Detected edges of serial intersectionally aligned brightfield sections. (D) Top row, 3D combined shape and intensity interpolated brightfield images; bottom row, 3D intensity interpolated fluorescence images. (E) 3D display of tumor boundary obtained from (D) (top row) and fluorescence intensities obtained from (D) (bottom row). Yellow grid, tumor boundary; red, fluorescence intensity.

Figure 8 shows a representative example of 2D registered MRI/MRSI, optical brightfield, fluorescence and H&E-stained images. Figure 8A shows a T_1-weighted MRI slice through the tumor, which was used to register the corresponding optical brightfield/fluorescence image to it. The segmented brightfield image with two fiducial markers by ASM is shown in Fig. 8B. Figure 8C displays the tumor shape-based rigid registered brightfield image with fiducial markers, and Fig. 8D shows the tumor shape-based warped brightfield image with fiducial markers. Figure 8E displays the corresponding warped H&E-stained necrotic core with registered straight fiducial markers segmented by active shape modeling. Figure 8F shows an overlay of Fig. 8A (red channel), Fig. 8D (green channel) and Fig. 8E (blue channel), displaying a yellow color where the MRI and brightfield images are overlaid, a cyan color where the brightfield and H&E-stained images are overlaid, and a white color where all three images are overlaid. The fiducial markers of optical brightfield images and H&E-stained images

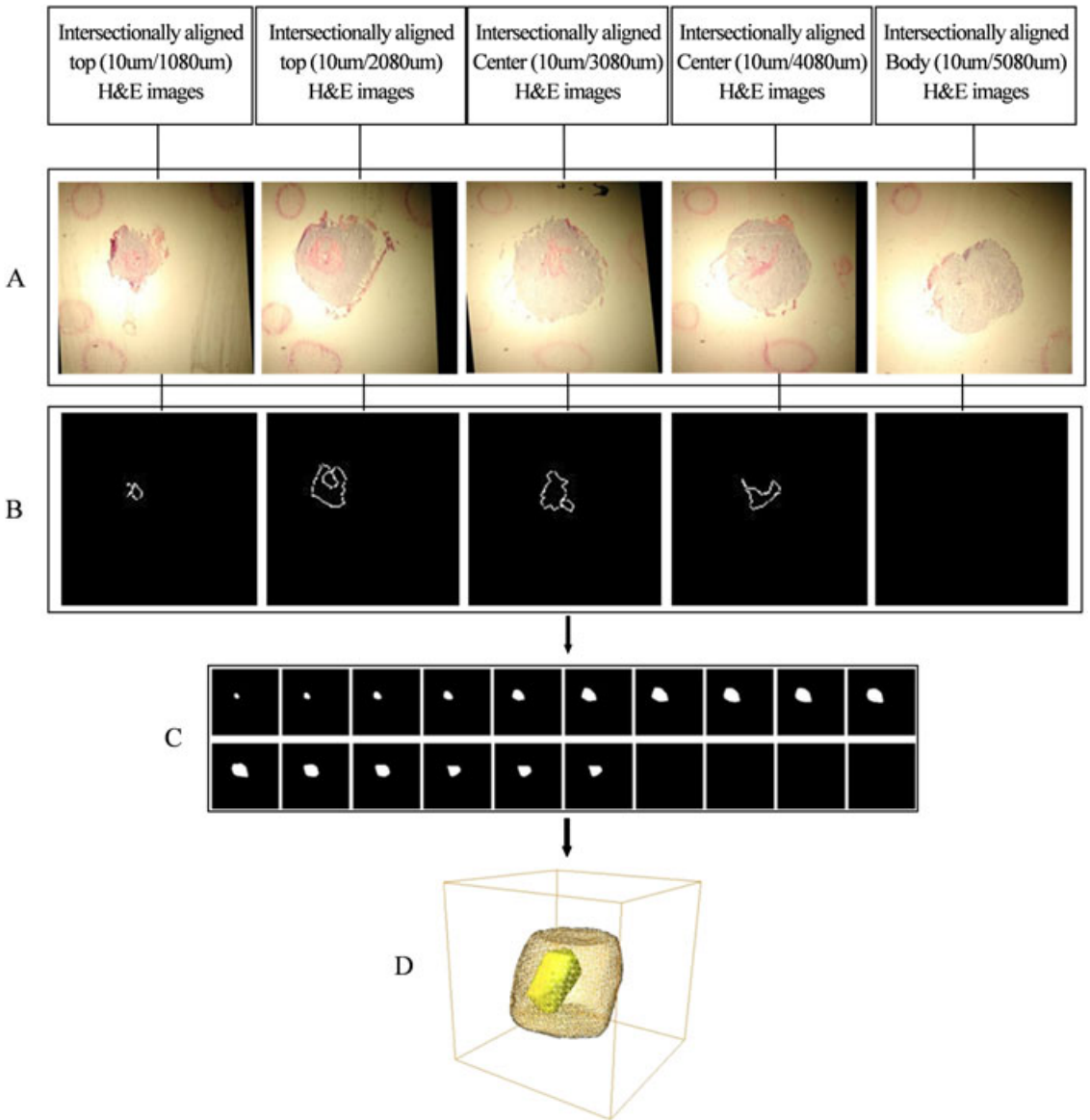

Figure 7. Results of three-dimensional (3D) reconstruction of hematoxylin and eosin (H&E)-stained histology images of 10-μm-thick tumor sections. (A) Histological serial sections after fiducial marker-based intersectional alignment. (B) Detected edges of necrotic regions from intersectionally aligned histological serial sections. (C) 3D shape interpolated images of necrotic region. (D) 3D display of tumor boundary from Fig. 6D (top row) and necrotic regions from (C). Yellow grid, tumor boundary; bright yellow, isosurface of the necrotic region.

were registered well. The tumor shape obtained from the brightfield images, which was registered to the tumor shape obtained from the corresponding MRI slice, matched well visually. The overhanging MRI boundary of the tumor, shown in red in Fig. 8F, originates from skin surrounding the tumor in the *in vivo* MRI scans. Figure 8G shows the nonrigid registered fluorescence image with the tumor boundary, and Fig. 8H shows the MRSI intensity map generated from the total choline-containing metabolites (tCho) signal.

Figure 9 shows an example of 3D registered MRI/MRSI, optical brightfield/fluorescence and H&E-stained histology images with fiducial markers, which were generated using our multimodal image reconstruction, registration and fusion platform. The boundary of a 3D T_1-weighted MRI dataset of a representative tumor is displayed as a yellow grid in Fig. 9A. Figure 9B shows the boundary of the tumor and fiducial markers of the corresponding MRI-registered optical brightfield imaging dataset as a blue isosurface. Figure 9C shows the corresponding H&E-stained necrotic core with registered straight fiducial markers displayed in green as a 3D isosurface. Figure 9D shows an overlay of Fig. 9A–C. The fiducial markers of optical brightfield images and H&E-stained images were registered well. The tumor shape in the brightfield images was registered to the tumor part of the corresponding MRI dataset (excluding the skin), and the two tumor shapes matched well visually, as shown in Fig. 9D. The boundary of the tumor obtained from the 3D MRI dataset, which is shown as the yellow grid in Fig. 9D, represents the surrounding skin of the tumor, and is therefore larger than the tumor boundary obtained from optical images, as these were obtained *ex vivo* after removal of the skin from the tumor. Figure 9E shows the tCho intensity map with tumor boundary. The registered fluorescence distribution is shown in red voltex

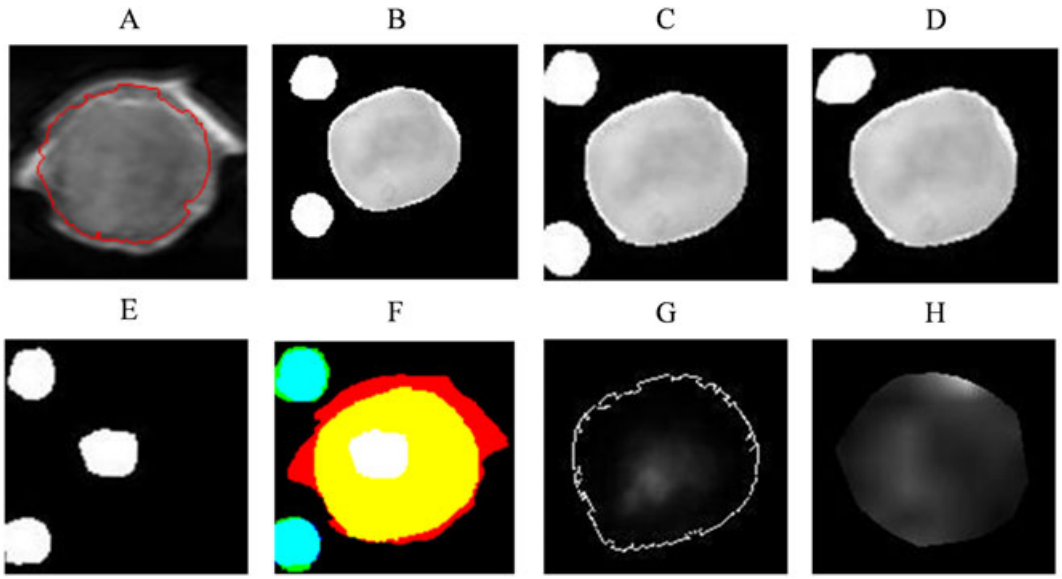

Figure 8. Two-dimensional (2D) registered MRI/MRSI and optical brightfield, fluorescence and hematoxylin and eosin (H&E)-stained images. (A) MRI T_1-weighted image with tumor edge detected by active shape model (ASM). (B) Segmented optical brightfield image with fiducial markers. (C) Rigid registered optical brightfield image with fiducial markers. (D) Combined rigid and nonrigid registered optical brightfield image with fiducial markers. (E) Registered H&E images with fiducial markers and the necrotic region. (F) Overlay of registered MRI, brightfield images and H&E images with fiducial markers (red channel, MRI; green channel, registered brightfield images; blue channel, registered H&E images; white, necrotic region from H&E image; yellow, overlay of MRI and brightfield images; cyan, overlay of brightfield image and H&E image). (G) Registered fluorescence image with tumor boundary. (H) Total choline-containing metabolites (tCho) intensity map; the region of interest of the tumor in tCho MRSI is generated by thresholding the water-unsuppressed MRSI water signal.

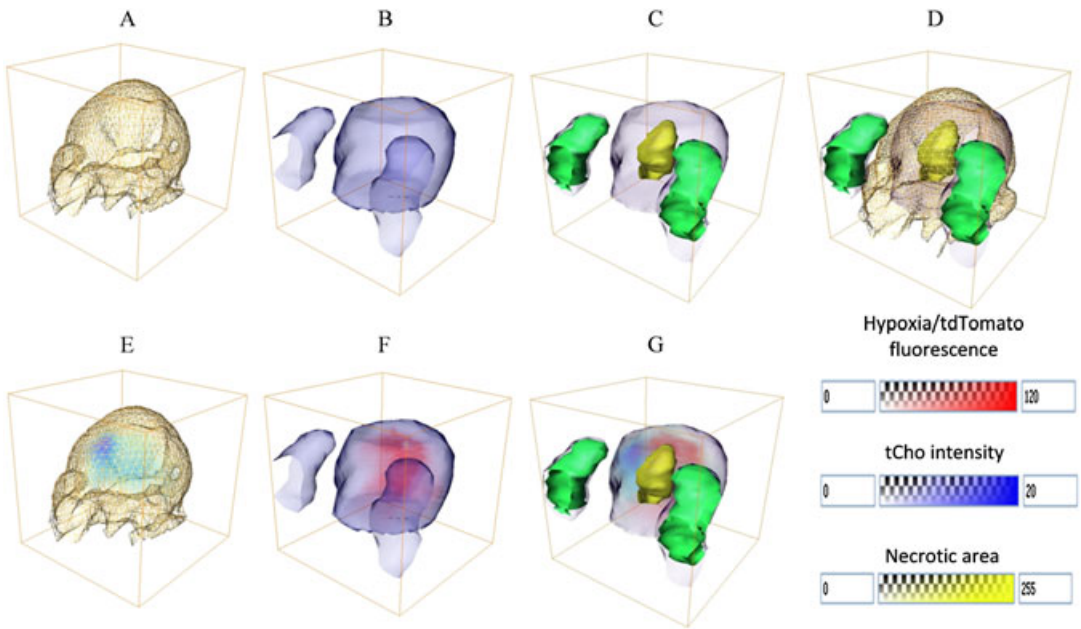

Figure 9. Three-dimensional (3D) registered MRI/MRSI, optical brightfield, fluorescence, and hematoxylin and eosin (H&E)-stained images. (A) Tumor boundary with skin obtained from 3D MRI T_1-weighted images (yellow grid). (B) Tumor boundary (blue isosurface) and fiducial markers (blue isosurface) from registered optical brightfield images. (C) Overlay of necrotic region from registered corresponding H&E-stained images (yellow transparent isosurface), registered straight fiducial markers displayed in 3D isosurface (green isosurface), registered optical tumor boundary (blue isosurface) and fiducial markers (blue isosurface) from brightfield images. (D) Overlay of (A)–(C). (E) 3D registered total choline-containing metabolites (tCho) map in blue voltex with tumor boundary from MRI in yellow gridline. (F) Registered fluorescence distribution in red voltex with tumor boundary (blue isosurface). (G) Fused tCho (light blue voltex), fluorescence (red voltex) and necrotic regions (yellow transparent isosurface) with fiducial markers from H&E-stained images (green isosurface) and tumor boundary (blue isosurface).

inside the tumor boundary in Fig. 9F. Figure 9G shows the fused tCho, fluorescence (hypoxic) and necrotic regions with fiducial markers and tumor boundary.

In preclinical cancer research performed in animal models, no gold standard imaging data are available to assess the accuracy of this method. However, mutual information is a standard method to measure the accuracy between different imaging modalities. The mutual information-based registration errors between MRI and optical brightfield images measured in four different tumors are shown in Fig. 10. The image difference error between MRI and original optical brightfield images was the highest. This difference error decreased after shape-based affine transformation was applied to the brightfield images. During the iterative warping of the brightfield images, this error continued to decrease and converged after several iterations. Each tumor shows a similar trend in this study, which demonstrates that this multimodal fusion strategy is feasible, robust and performs well.

DISCUSSION

We have developed a versatile multimodal image reconstruction and fusion platform which can be applied to a wide range of combined *in vivo* and *ex vivo* imaging modalities in preclinical cancer research and, potentially, in clinical applications. We have successfully demonstrated the performance of this software platform in an example of combined MRI/MRSI, brightfield/fluorescence and histology imaging of a human breast tumor xenograft model, which expressed tdTomato fluorescent protein in hypoxic tumor regions. The workflow of this 3D reconstruction and fusion platform includes a fiducial marker system that helps register and reconstruct different *ex vivo* imaging datasets. Following successful image reconstruction, registration and fusion with our software platform, co-localization or correlation analysis, such as principal component analysis and canonical correlation analysis of metabolites, fluorescent proteins and necrotic or IHC-positive regions, can be performed to extract the spatial features of the probed molecular processes. In the future, we will use this platform to investigate effects of the tumor microenvironment on MRS-detectable metabolites and the underlying molecular pathways in human breast tumor xenograft models.

To our knowledge, it is impossible for the presented 3D reconstruction and registration to be reliably performed without fiducial markers. As tumor slices are typically moved inconsistently from section to section during sectioning procedures, the 3D volume of a tumor or features inside the tumor in optical and histologic images will be inaccurate without fiducial markers. Unlike previously described fiducial marker systems in small rodents (25–27), an external nondestructive fiducial marker strategy was developed in this study. Our marker system was embedded into gelatin, and not directly into the tissue of interest itself, as suggested previously (25–27), which avoids contamination and deformation of the tissue under investigation. As gelatin, compared with the wax used in ref. (28), is of a comparable solidity and consistency as tumors, shear forces and the local deformation of tissue and markers during sectioning are similar. These fiducial markers were applied in both *ex vivo* brightfield/fluorescence imaging and *ex vivo* histology imaging, but not in MRI/MRSI, because gelatin embedding of a skin-covered tumor in a live mouse throughout a 1–2-h MRI/MRSI acquisition was not feasible because of the limited size of the radiofrequency coil in the animal MRI scanner and drying out of the gelatin during this time period. We therefore performed a tumor shape-based 3D registration of the MRI/MRSI datasets with the brightfield/fluorescence and histology imaging datasets.

The segmentation of each marker and tumor boundary was performed semi-automatically using the ASM and by manually

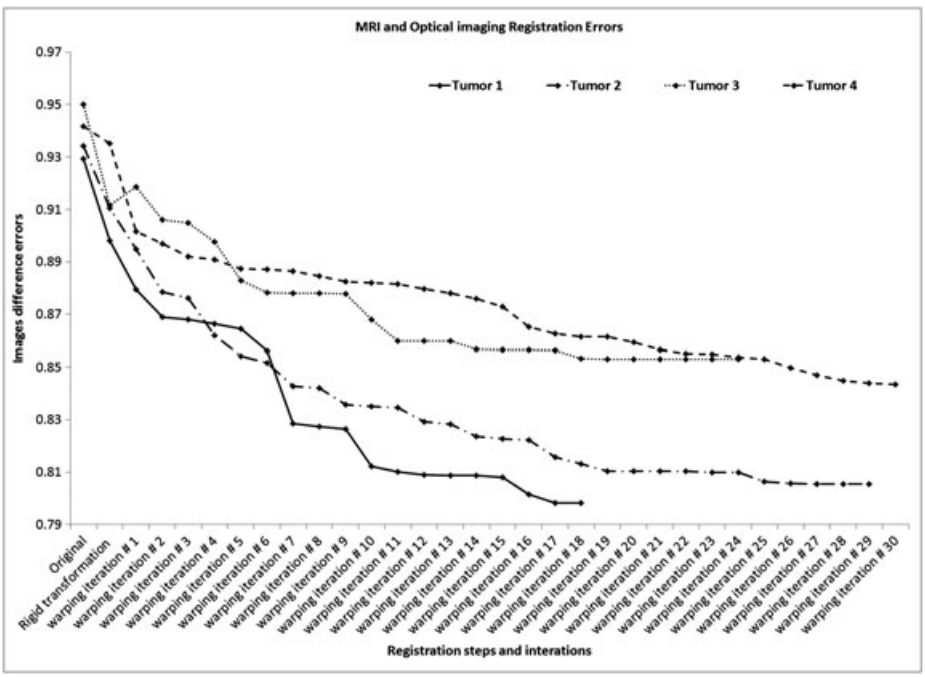

Figure 10. Convergence properties of registration of MRI and optical image distances in each registration step of four different tumors. The image difference error is the mutual information error between two imaging modalities and, after each registration step, this mutual information error was minimized.

setting a series of initial boundary points on each 2D slice. The average segmentation time of each 2D slice was around 40 s, including the manual selection of the boundary points. The tumor shape varies greatly; thus, fully automated segmentation, such as thresholding or histogram-based methods, may increase the registration error, which is why this semi-automated segmentation approach fits this application well. Moreover, the addition of *b*-spline-based warping further reduced the registration errors. This method can visualize single volumes of necrosis inside the tumor. It is also possible to semi-manually use the same method to perform 3D reconstruction of separate small necrotic regions in the tumor, and then add them together. The number of slices for interpolation is still justifiable for such an approach.

Shrinkage of tumor tissue following cryosectioning and histologic or IHC staining is a common problem when comparing histologic or IHC sections with *in vivo* MRI data of the same tumor (56); therefore, the tumor boundary in our histology datasets cannot be used directly for registration. To avoid this problem, we used the fiducial markers to register histology with MRI via the fresh 2-mm-thick sections imaged with brightfield microscopy as an intermediate modality. As these 2-mm-thick sections are fresh tissue without fixation, and are thicker than the histology sections (10 μm), they preserve the original geometric information of the tumor very well with the embedded fiducial markers after sectioning.

We performed an average in-plane spatial transformation between corresponding MRI and 3D microscopic image slices to obtain 3D registered microscopic brightfield and fluorescence images. The difference in the angulation of MRI slices and the cutting plane of 2-mm-thick sections could potentially lead to a matching problem. However, the positioning of tumor-bearing mice during our MR measurements was kept the same as in the sectioning process, which dramatically reduced the registration error.

Recently, Chappelow *et al*. (57) have demonstrated an elastic registration of multiparametric prostate MRI and histology by multi-attribute combined mutual information (MACMI) in human prostate cancer. Multiprotocol MRI data obtained from clinical prostate cancers were used in this method. Although the MACMI algorithm provides an automated approach for the registration of multiparametric MRI data with histology, this approach cannot be extended to the incorporation of additional imaging modalities, such as fluorescence imaging, and relies on the availability of multiparametric datasets from MRI. In other applications, such as diffusion or permeability studies of tumors, a contrast agent can be used during MRI acquisition to provide additional spatially resolved information on structures such as, for example, vascular structures, which could be obtained from inside the tumor. The registration of MRI and optical images could be completed using this additional structural information, and not solely the tumor boundary information, which may lead to a more accurate registration.

Our framework is not limited to preclinical breast cancer research and the presented imaging modalities, and can be adapted to clinical breast cancer applications involving any type of multimodal imaging approach combined with histology and/or IHC. Clinically, residual tumor after excisional biopsy has been reported in 32–63% of breast cancer cases (58–60). These patients undergo contrast-enhanced MRI before re-excision lumpectomy or mastectomy is performed, followed by histopathologic evaluation of the excised tissue. The information obtained from both MRI and histopathologic images is important in guiding the re-excision surgery. As a result, the combination of *in vivo* MRI, *ex vivo* optical histology and/or IHC imaging and extracting information from both modalities becomes necessary, and could benefit from our 3D reconstruction and fusion platform. Human biopsy samples can be much larger than preclinical mouse samples. Using the concept of 2-mm-thick optical images as an intermediate imaging step could lead to more accurate 3D reconstruction and registration of MRI and histologic data. More automated tumor boundary detection methods may be necessary to speed up the processing, imaging and validation time for clinical applications.

Our multimodal, multiscale, molecular imaging platform is not limited to *in vivo* MRI/MRSI, *ex vivo* optical brightfield/fluorescence imaging and histology and/or IHC imaging. Another promising *ex vivo* modality that could be included in the presented 3D imaging workflow is MSI of tumors to additionally detect the spatial distribution of a wide variety of biomolecules (61). Gelatin has also been shown to facilitate MSI of breast cancer tissue (61). MSI data can be obtained from adjacent sections of histology or IHC data, and this presented multimodal, multiscale, molecular imaging platform can be expanded to include MSI.

Acknowledgements

We thank Dr Vaddapuram P. Chacko for expert technical support with the MRI studies on the Bruker 9.4-T Small Animal Scanner. We thank Dr Zaver M. Bhujwalla for useful discussions.

This work was supported by a National Institutes of Health (NIH) grant R01 CA134695.

REFERENCES

1. Glunde K, Pathak AP, Bhujwalla ZM. Molecular-functional imaging of cancer: to image and imagine. Trends Mol. Med. 2007; 13: 287–297.
2. Penet MF, Mikhaylova M, Li C, Krishnamachary B, Glunde K, Pathak AP, Bhujwalla ZM. Applications of molecular MRI and optical imaging in cancer. Future Med. Chem. 2010; 2: 975–988.
3. Lauterbu PC. Image formation by induced local interactions – examples employing nuclear magnetic-resonance. Nature 1973; 242: 190–191.
4. Ronald JA, Chen YX, Belisle AJL, Hamilton AM, Rogers KA, Hegele RA, Misselwitz B, Rutt BK. Comparison of gadofluorine-M and Gd-DTPA for noninvasive staging of atherosclerotic plaque stability using MRI. Circ. Cardiovasc. Imaging 2009; 2: 226–234.
5. Partridge SC, Gibbs JE, Lu Y, Esserman LJ, Tripathy D, Wolverton DS, Rugo HS, Hwang ES, Ewing CA, Hylton NM. MRI measurements of breast tumor volume predict response to neoadjuvant chemotherapy and recurrence-free survival. Am. J. Roentgenol. 2005; 184: 1774–1781.
6. Brigger I, Dubernet C, Couvreur P. Nanoparticles in cancer therapy and diagnosis. Adv. Drug Deliv. Rev. 2002; 54: 631–651.
7. Glunde K, Artemov D, Penet MF, Jacobs MA, Bhujwalla ZM. Magnetic resonance spectroscopy in metabolic and molecular imaging and diagnosis of cancer. Chem. Rev. 2010; 110: 3043–3059.
8. Penet MF, Pathak AP, Raman V, Ballesteros P, Artemov D, Bhujwalla ZM. Noninvasive multiparametric imaging of metastasis-permissive microenvironments in a human prostate cancer xenograft. Cancer Res. 2009; 69: 8822–8829.
9. Nielsen FU, Daugaard P, Bentzen L, Stodkilde-Jorgensen H, Overgaard J, Horsman MR, Maxwell RJ. Effect of changing tumor oxygenation on glycolytic metabolism in a murine C3H mammary carcinoma assessed by *in vivo* nuclear magnetic resonance spectroscopy. Cancer Res. 2001; 61: 5318–5325.
10. Aboagye EO, Bhujwalla ZM. Malignant transformation alters membrane choline phospholipid metabolism of human mammary epithelial cells. Cancer Res. 1999; 59: 80–84.

11. Opstad KS, Bell BA, Griffiths JR, Howe FA. An investigation of human brain tumour lipids by high-resolution magic angle spinning ^{1}H MRS and histological analysis. NMR Biomed. 2008; 21: 677–685.
12. Greijer AE, van der Groep P, Kemming D, Shvarts A, Semenza GL, Meijer GA, van de Wiel MA, Belien JA, van Diest PJ, van der Wall E. Up-regulation of gene expression by hypoxia is mediated predominantly by hypoxia-inducible factor 1 (HIF-1). J. Pathol. 2005; 206: 291–304.
13. Burnett CA, Xie J, Quijano J, Shen Z, Hunter F, Bur M, Li KC, Danthi SN. Synthesis, *in vitro*, and *in vivo* characterization of an integrin alpha(v) beta(3)-targeted molecular probe for optical imaging of tumor. Bioorg. Med. Chem. 2005; 13: 3763–3771.
14. Jin ZH, Josserand V, Foillard S, Boturyn D, Dumy P, Favrot MC, Coll JL. *In vivo* optical imaging of integrin alphaV-beta3 in mice using multivalent or monovalent cRGD targeting vectors. Mol. Cancer 2007; 6: 41.
15. Smith-Jones PM, Solit DB, Akhurst T, Afroze F, Rosen N, Larson SM. Imaging the pharmacodynamics of HER2 degradation in response to Hsp90 inhibitors. Nat. Biotechnol. 2004; 22: 701–706.
16. Yeung SJ, Pan J, Lee MH. Roles of p53, MYC and HIF-1 in regulating glycolysis – the seventh hallmark of cancer. Cell. Mol. Life Sci. 2008; 65: 3981–3999.
17. Gocheva V, Joyce JA. Cysteine cathepsins and the cutting edge of cancer invasion. Cell Cycle 2007; 6: 60–64.
18. Federman S, Miller LM, Sagi I. Following matrix metalloproteinases activity near the cell boundary by infrared micro-spectroscopy. Matrix Biol. 2002; 21: 567–577.
19. Bremer C, Bredow S, Mahmood U, Weissleder R, Tung CH. Optical imaging of matrix metalloproteinase-2 activity in tumors: feasibility study in a mouse model. Radiology 2001; 221: 523–529.
20. Dadiani M, Kalchenko V, Yosepovich A, Margalit R, Hassid Y, Degani H, Seger D. Real-time imaging of lymphogenic metastasis in orthotopic human breast cancer. Cancer Res. 2006; 66: 8037–8041.
21. Hsiung PL, Phatak DR, Chen Y, Aguirre AD, Fujimoto JG, Connolly JL. Benign and malignant lesions in the human breast depicted with ultrahigh resolution and three-dimensional optical coherence tomography. Radiology 2007; 244: 865–874.
22. Wang J, Jiang S, Li Z, diFlorio-Alexander RM, Barth RJ, Kaufman PA, Pogue BW, Paulsen KD. *In vivo* quantitative imaging of normal and cancerous breast tissue using broadband diffuse optical tomography. Med. Phys. 2010; 37: 3715–3724.
23. Chen Y, Yuan SA, Wierwille J, Naphas R, Li QA, Blackwell TR, Winnard PT, Raman V, Glunde K. Integrated optical coherence tomography (OCT) and fluorescence laminar optical tomography (FLOT). IEEE J. Selected Top. Quantum Electron. 2010; 16: 755–766.
24. Coons AH, Creech HJ, Jones RN. Immunological properties of an antibody containing a fluorescent group. Proc. Soc. Exp. Biol. Med. 1941; 47: 200–202.
25. Humm JL, Ballon D, Hu YC, Ruan S, Chui C, Tulipano PK, Erdi A, Koutcher J, Zakian K, Urano M, Zanzonico P, Mattis C, Dyke J, Chen Y, Harrington P, O'Donoghue JA, Ling CC. A stereotactic method for the three-dimensional registration of multi-modality biologic images in animals: NMR, PET, histology, and autoradiography. Med. Phys. 2003; 30: 2303–2314.
26. Cho H, Ackerstaff E, Carlin S, Lupu ME, Wang Y, Rizwan A, O'Donoghue J, Ling CC, Humm JL, Zanzonico PB, Koutcher JA. Noninvasive multimodality imaging of the tumor microenvironment: registered dynamic magnetic resonance imaging and positron emission tomography studies of a preclinical tumor model of tumor hypoxia. Neoplasia 2009; 11: 247–259.
27. McGrath DM, Vlad RM, Foltz WD, Brock KK. Technical note: fiducial markers for correlation of whole-specimen histopathology with MR imaging at 7 tesla. Med. Phys. 2010; 37: 2321–2328.
28. Breen MS, Lazebnik RS, Wilson DL. Three-dimensional registration of magnetic resonance image data to histological sections with model-based evaluation. Ann. Biomed. Eng. 2005; 33: 1100–1112.
29. Dauguet J, Delzescaux T, Conde F, Mangin JF, Ayache N, Hantraye P, Frouin V. Three-dimensional reconstruction of stained histological slices and 3D non-linear registration with *in-vivo* MRI for whole baboon brain. J. Neurosci. Methods 2007; 164: 191–204.
30. Kim B, Boes JL, Frey KA, Meyer CR. Mutual information for automated unwarping of rat brain autoradiographs. Neuroimage 1997; 5: 31–40.
31. Mega MS, Chen SS, Thompson PM, Woods RP, Karaca TJ, Tiwari A, Vinters HV, Small GW, Toga AW. Mapping histology to metabolism: coregistration of stained whole-brain sections to premortem PET in Alzheimer's disease. Neuroimage 1997; 5: 147–153.
32. Ourselin S, Roche A, Subsol G, Pennec X, Ayache N. Reconstructing a 3D structure from serial histological sections. Image Vision Comput. 2001; 19: 25–31.
33. Toga AW, Ambach KL, Schluender S. High-resolution anatomy from in situ human brain. Neuroimage 1994; 1: 334–344.
34. Chakravarty MM, Bertrand G, Hodge CP, Sadikot AF, Collins DL. The creation of a brain atlas for image guided neurosurgery using serial histological data. Neuroimage 2006; 30: 359–376.
35. Malandain G, Bardinet E, Nelissen K, Vanduffel W. Fusion of autoradiographs with an MR volume using 2-D and 3-D linear transformations. Neuroimage 2004; 23: 111–127.
36. Glunde K, Guggino SE, Solaiyappan M, Pathak AP, Ichikawa Y, Bhujwalla ZM. Extracellular acidification alters lysosomal trafficking in human breast cancer cells. Neoplasia 2003; 5: 533–545.
37. Raman V, Artemov D, Pathak AP, Winnard PT Jr, McNutt S, Yudina A, Bogdanov A Jr, Bhujwalla ZM. Characterizing vascular parameters in hypoxic regions: a combined magnetic resonance and optical imaging study of a human prostate cancer model. Cancer Res. 2006; 66: 9929–9936.
38. Krishnamachary B, Penet MF, Nimmagadda S, Mironchik Y, Raman V, Solaiyappan M, Semenza GL, Pomper M, Bhujwalla ZM. Hypoxia regulates CD44 and its variant isoforms through HIF-1α in MDA-MB-231 human breast cancer cells and tumors. PLOS One, 2012. In Press
39. Glunde K, Shah T, Winnard PT Jr, Raman V, Takagi T, Vesuna F, Artemov D, Bhujwalla ZM. Hypoxia regulates choline kinase expression through hypoxia-inducible factor-1 alpha signaling in a human prostate cancer model. Cancer Res. 2008; 68: 172–180.
40. Goelman G, Prammer MG. The CPMG pulse sequence in strong magnetic-field gradients with applications to oil-well logging. J. Magn. Reson. Ser. A 1995; 113: 11–18.
41. Hurlimann MD, Griffin DD. Spin dynamics of Carr–Purcell–Meiboom–Gill-like sequences in grossly inhomogeneous B-0 and B-1 fields and application to NMR well logging. J. Magn. Reson. 2000; 143: 120–135.
42. Brown TR, Kincaid BM, Ugurbil K. NMR chemical shift imaging in three dimensions. Proc. Natl. Acad. Sci. USA 1982; 79: 3523–3526.
43. Tkac I, Starcuk Z, Choi IY, Gruetter R. *In vivo* ^{1}H NMR spectroscopy of rat brain at 1 ms echo time. Magn. Reson. Med. 1999; 41: 649–656.
44. Cootes TF, Taylor CJ, Cooper DH, Graham J. Active shape models – their training and application. Comput Vis Image Und 1995; 61: 38–59.
45. Cootes TF, Edwards GJ, Taylor CJ. Active appearance models. IEEE Trans. Pattern Anal. Machine Intell. 2001; 23: 681–685.
46. Cootes TF, Taylor CJ. Constrained active appearance models. *Proceedings of the Eighth IEEE International Conference on Computer Vision*, Vol. I, Vancouver, BC, Canada, 2001: 748–754.
47. Xu C, Prince JL. Snakes, shapes, and gradient vector flow. IEEE Trans. Image Process. 1998; 7: 359–369.
48. Frenkel KA. Volume rendering. Commun. ACM 1989; 32: 426–435.
49. Udupa JK, Herman GT. Volume rendering versus surface rendering. Commun. ACM 1989; 32: 1364–1366.
50. Du Q, Wang XQ. Centroidal Voronoi tessellation based algorithms for vector fields visualization and segmentation. *Proceedings of IEEE Visualization 2004*, Austin, TX, USA, 2004: 43–50.
51. Romano-Diaz E, van de Weygaert R. Delaunay tessellation field estimator analysis of the PSCz local universe: density field and cosmic flow. Monthly Notices R Astronom. Soc. 2007; 382: 2–28.
52. Lee S, Wolberg G, Shin SY. Scattered data interpolation with multilevel B-splines. IEEE Trans Visual Comput Graph 1997; 3: 228–244.
53. Rueckert D, Sonoda LI, Hayes C, Hill DLG, Leach MO, Hawkes DJ. Non-rigid registration using free-form deformations: application to breast MR images. IEEE Trans. Med. Imaging 1999; 18: 712–721.
54. Oguro S, Tokuda J, Elhawary H, Haker S, Kikinis R, Temparly CMC, Hata N. MRI signal intensity based b-spline nonrigid registration for pre- and intraoperative imaging during prostate brachytherapy. J. Magn. Reson. Imaging 2009; 30: 1052–1058.

55. Studholme C, Hill DLG, Hawkes DJ. An overlap invariant entropy measure of 3D medical image alignment. Pattern Recog. 1999; 32: 71–86.
56. Jacobs MA, Windham JP, Soltanian-Zadeh H, Peck DJ, Knight RA. Registration and warping of magnetic resonance images to histological sections. Med. Phys. 1999; 26: 1568–1578.
57. Chappelow J, Bloch BN, Rofsky N, Genega E, Lenkinski R, DeWolf W, Madabhushi A. Elastic registration of multimodal prostate MRI and histology via multiattribute combined mutual information. Med. Phys. 2011; 38: 2005–2018.
58. Lee JM, Orel SG, Czerniecki BJ, Solin LJ, Schnall MD. MRI before reexcision surgery in patients with breast cancer. Am. J. Roentgenol. 2004; 182: 473–480.
59. Orel SG, Rosen M, Mies C, Schnall MD. MR imaging-guided 9-gauge vacuum-assisted core-needle breast biopsy: initial experience. Radiology 2006; 238: 54–61.
60. Kim JA, Son EJ, Kim EK, Kim MJ, Kwak JY, Jeong J. Postexcisional breast magnetic resonance imaging in patients with breast cancer: predictable findings of residual cancer. J. Comput. Assist. Tomogr. 2009; 33: 940–945.
61. Amstalden van Hove ER, Blackwell TR, Klinkert I, Eijkel GB, Heeren RM, Glunde K. Multimodal mass spectrometric imaging of small molecules reveals distinct spatio-molecular signatures in differentially metastatic breast tumor models. Cancer Res. 2010; 70: 9012–9021.